ADVANCED ENERGY MATERIALS
www.advenergymat.de

Ammonia Synthesis over Ruthenium Supported on Metastable Perovskite Oxyhydrides Ba*RE*O_2H (*RE* = Y, Sc) Prepared by Mechanochemical Method

Shun Sato, Masayoshi Miyazaki, Satoru Matsuishi, Hideo Hosono,* and Masaaki Kitano**

Oxyhydrides have attracted attention as materials with various unique properties derived from lattice hydride ions (H^-). However, their instability makes synthesis by conventional thermal synthesis methods difficult, so an appropriate synthesis strategy is required. Here, the mechanochemical synthesis of perovskite oxyhydrides Ba*RE*O_2H (*RE* = Y, Sc) for catalyst applications is reported. The formation of $BaYO_2H$ is known to be thermodynamically unstable; however, a mechanochemical process that inevitably proceeds under non-equilibrium conditions enables the synthesis of such a metastable oxyhydride material without any heat treatment. Furthermore, $BaScO_2H$, which is typically obtained at very high temperatures (1000 °C) and pressure (>4 GPa), is successfully synthesized at room temperature by the mechanochemical method. The ammonia synthesis reaction over these oxyhydrides supporting Ru is significantly enhanced at low temperatures, and the ammonia synthesis rates are significantly higher than conventional oxide-supported Ru catalysts. The mechanochemically synthesized Ba*RE*O_2H has many anionic electrons with low work function at the site of H^- vacancies, which enables strong electron donation to Ru and the storage of excess hydrogen adatoms from the Ru surface that results in high catalytic performance.

1. Introduction

Oxyhydrides, in which oxide ions (O^{2-}) and hydride ions (H^-) form an anion sublattice, are novel inorganic compounds that have attracted attention in the field of materials science due to their unique ionic conductivity, fluorescence properties, and catalytic properties.[1–4] These properties are mainly due to the unique coordination environment and the specific chemical and physical properties of H^-, while O^{2-} is responsible for the construction and stabilization of the crystal framework. Oxyhydrides can be synthesized by H^- doping of typical oxides such as $BaTiO_{3-x}H_x$ and $LaH_{3-2x}O_x$ by exploiting the similar ionic radius of O^{2-} and H^- (135 pm).[5–7] It is also possible to obtain novel compounds with unique chemical compositions, such as La_2LiHO_3 and A_3MO_4H (A = Rb, Cs; M = Mo, W), which allows for a wide variety of material designs.[8,9] Although a number of oxyhydrides have been predicted by theoretical calculations, it is difficult to synthesize oxyhydrides by conventional high-temperature solid-state reactions because of the chemical and thermal instability of H^-. On the other hand, it has been reported that high-pressure synthesis and topochemical reactions are effective for the synthesis of oxyhydride materials.[10] The most advantageous point of high-pressure synthesis is the capability to confine hydrogen in the solid phase by ultra-high external pressure (2–8 GPa), which allows hydrogen to react and remain as H^- even at high temperatures (800–1200 °C) if the sample is oxygen deficient. In some cases, crystal phases known as pressure-stabilized phases,

S. Sato, M. Miyazaki, H. Hosono, M. Kitano
MDX Research Center for Element Strategy
International Research Frontiers Initiative
Tokyo Institute of Technology
4259 Nagatsuta, Midori-ku, Yokohama 226–8503, Japan
E-mail: hosono@mces.titech.ac.jp; kitano.m.aa@m.titech.ac.jp

The ORCID identification number(s) for the author(s) of this article can be found under https://doi.org/10.1002/aenm.202402353

DOI: 10.1002/aenm.202402353

S. Matsuishi, H. Hosono
Research Center for Materials Nanoarchitectonics
National Institute for Materials Science
1-1 Namiki, Tsukuba, Ibaraki 305-0044, Japan
E-mail: matsuishi.satoru@nims.go.jp

M. Kitano
Advanced Institute for Materials Research (WPI-AIMR)
Tohoku University
Sendai 980–8577, Japan

which form only above critical pressure, are obtained under high-pressure conditions. Topochemical reactions are typically conducted at low temperatures (<600 °C) by the reaction of host oxide materials with hydride materials such as CaH_2 over a long time (>50 h). This technique limits cation diffusion at low temperatures so that the lattice O^{2-} ions can be replaced by H^- without changes in the crystal framework of the oxide.

However, some compounds have been reported to be impossible to synthesize by these methods, such as $BaYO_2H$. $BaYO_2H$ has been predicted to be within 100 meV per atom from the convex hull based on a machine-learning model that assumes the formation of a tetragonal perovskite structure.[11] Ba_2YO_3H with a K_2NiF_4-type structure has been produced by high-pressure synthesis (4 GPa)[12]; however, the high-pressure synthesis of $BaYO_2H$ has not been reported to date. It is also difficult to synthesize $BaYO_2H$ by topochemical reaction due to the difficulty of producing the metastable $Ba_2Y_2O_5$ precursor as a pure phase without any impurities.[13] It is important to overcome such metastability of oxyhydrides in developing new materials, which requires constructing a suitable synthesis strategy. Therefore, we have adopted mechanochemical methods in which chemical reactions are induced by mechanical energy under non-equilibrium conditions as an effective method for synthesizing oxyhydrides. The accumulation of strain energy generates a high-energy intermediate state in the material, whereby metastable phases with high Gibbs free energies can be formed.[14] Mechanochemical methods have been conventionally used to synthesize metastable alloys and hydrides, and there have been some reports on the synthesis of multi-anionic hydrides in recent years.[15,16] There have also been several reports on the synthesis of oxyhydrides such as $BaTiO_{3-x}H_x$, $Sr_5(PO_4)_3H$, and $Sr_5(BO_3)_3H$, which shows the significant potential of this method for the synthesis of metastable oxyhydrides.[17–19]

Here, we report the mechanochemical synthesis of a metastable perovskite oxyhydride, $BaYO_2H$, and $BaScO_2H$, and their catalytic activity for NH_3 synthesis. Since the powder samples obtained by mechanochemical methods are expected to exhibit excellent catalytic activity and ionic conductivity at their surfaces and grain boundaries,[20] revealing their functions at the interfaces is an important issue in evaluating the availability of the oxyhydrides obtained by mechanochemical methods. Most recently, the mechanochemical synthesis of perovskite oxyhydrides, including these two oxyhydrides, have been reported before our report.[21] The paper reported a relationship between the feasibility of mechanochemical reactions and the calculated shear modulus of the starting reagents, while there is no application based on the interfacial or surface properties of these oxyhydrides. In the present work, the catalytic properties toward ammonia synthesis are examined for Ru catalysts supported on the synthesized Ba*RE*O_2H (*RE* = Y, Sc) and compared with those of Ru-loaded oxides with the same cation composition and other reported oxyhydride-based catalysts. In addition, the surface structure of Ru/Ba*RE*O_2H is investigated in detail to clarify the role of lattice H^- ions. In this catalyst system, hydride-deficient interfaces specifically generated by mechanochemical methods contribute to catalytic performance.

2. Results

2.1. Synthesis and Characterization of Ba*RE*O_2H

Figure 1a shows powder XRD patterns for the oxyhydrides after mechanochemical synthesis. The XRD patterns for the samples just after mechanochemical milling of a mixture of the precursors were simple due to the cubic perovskite structure, and no peak splitting or other peaks due to impurity phases were observed. The resultant materials were heated at 500 °C for 72 h under vacuum to improve the crystallinity for Rietveld analysis. The structural data for $BaScO_2H$ obtained from ICSD (No.257866) were used to refine the XRD patterns, and in the case of $BaYO_2H$, the Sc symbol in this data was replaced by the Y symbol (Tables S1 and S2, Supporting Information). As shown in Figure 1b,c, the main peaks for both samples are well-fitted to Ba*RE*O_2H with a cubic perovskite structure (*Pm*-3*m*). There were no impurities in the $BaYO_2H$ sample, while small impurity peaks were observed only for the $BaScO_2H$ sample. The refined phase fractions for the $BaScO_2H$ sample indicate that the perovskite phase contributes 98.5 wt.%, whereas the Sc_2O_3 phase remains at 1.5 wt.%. The refined lattice parameters for Ba*RE*O_2H are summarized in **Table 1**. The lattice constant for $BaScO_2H$ (a = 4.1468(2) Å) is close to the reported value (a = 4.15034(3) Å) within an error of less than 0.1%.[22] The volume of the unit cell for $BaYO_2H$ is ≈1.14 times larger than that for $BaScO_2H$, which is close to the volume expansion rate (15.0%) observed in $GdFeO_3$-type orthorhombic perovskite La*RE*O_3 (*RE* = Sc, Y).[23,24] Ba*RE*$O_{3-\delta}$ with the same crystal structure and cation composition as Ba*RE*O_2H was synthesized by the mechanochemical method using only oxide precursors (Figure S1, Supporting Information). The lattice constant for $BaScO_{3-\delta}$ (a = 4.132(2) Å) is similar to that reported for $BaScO_{3-\delta}$ (a = 4.13 Å) obtained by firing $Ba_3Sc_2(OH)_{12}$.[25] The larger lattice constant for Ba*RE*O_2H than for Ba*RE*$O_{3-\delta}$ can be understood by the introduction of H^- into the lattice, i.e., H^- with the same ionic size as O^{2-} (135 pm)[7] occupies the oxygen vacancy sites in oxygen-deficient cubic perovskite Ba*RE*$O_{3-\delta}$ to form Ba*RE*O_2H.

TDS measurements were conducted to determine the amount of H^- in the oxyhydrides. Two H_2 desorption peaks (m/z = 2) were observed in the TDS profiles for $BaYO_2H$ (**Figure 2a**) ≈150 °C and above 300 °C. The sharp desorption peak ≈150 °C is attributed to the H_2 desorption from the surface, whereas the broad desorption peaks above 300 °C are the desorption of hydrogen from bulk since the diffusion of bulk H^- ion to the surface requires higher temperature. Signals with m/z = 18 were also observed below 400 °C, attributed to H_2O physically adsorbed on the sample holder and the sample's surface. However, the intensity of the H_2O signal was only ≈1/100 that of the H_2 signal. $BaScO_2H$ showed desorption profiles similar to those for $BaYO_2H$ (Figure 2b). These results suggest that hydrogen exists in similar environments in the crystals of both compounds.

Table 1. Refined lattice constants for Ba*RE*O_2H and Ba*RE*$O_{3-\delta}$.

	$BaYO_2H$	$BaYO_{3-\delta}$	$BaScO_2H$	$BaScO_{3-\delta}$
a (Å)	4.3294(5)	4.2979(7)	4.1468(2)	4.132(2)

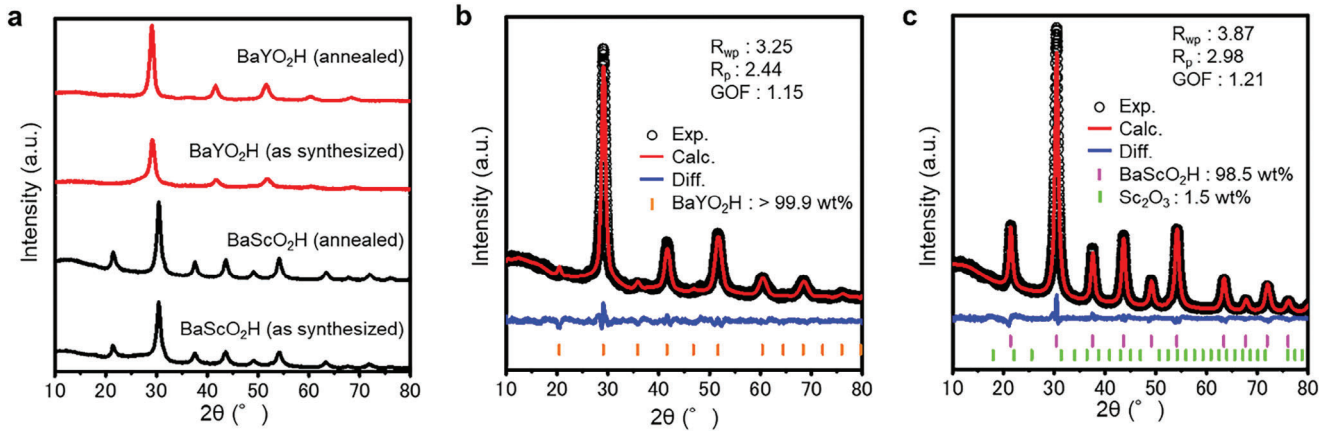

Figure 1. Crystal structure analysis of Ba*RE*O$_2$H. a) XRD patterns for Ba*RE*O$_2$H before and after heat treatment. Experimental XRD patterns and Rietveld refinement for b) BaYO$_2$H and c) BaScO$_2$H samples after heat treatment.

The amounts of H_2 released from BaYO$_2$H and BaScO$_2$H were 1.12 and 1.06 mmol g^{-1}, respectively. The chemical composition was estimated to be BaYO$_2$H$_{0.58}$ and BaScO$_2$H$_{0.46}$, which suggests that the obtained oxyhydrides contain significant amounts of H^- vacancies. When anion vacancies are formed, optical absorption of low-energy light should be observed, and the sample was gray in color (Figure S2, Supporting Information). The sample color is caused by the broad and weak absorption band ≈1.7–3.5 eV (Figure S3, Supporting Information). This band is similar to the simulated optical absorption spectra of H-deficient models

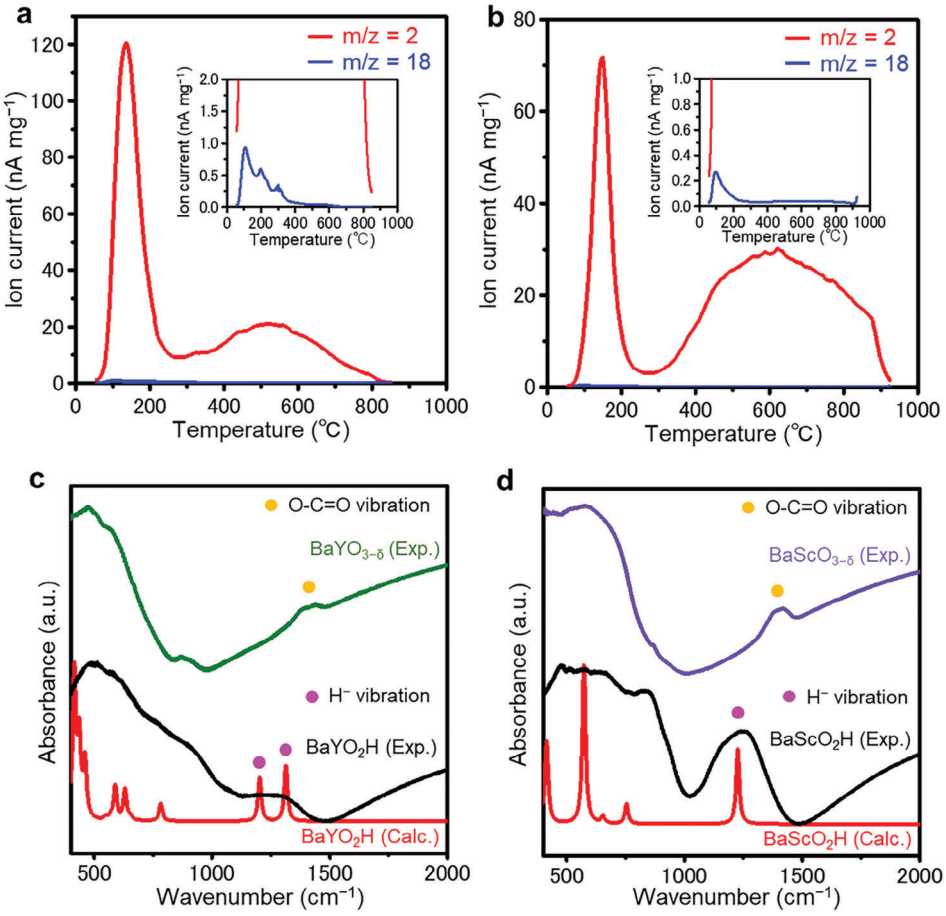

Figure 2. Detection and quantification of hydrogen incorporated in Ba*RE*O$_2$H. TDS spectra of a) BaYO$_2$H and b) BaScO$_2$H. c) FT-IR spectra of BaYO$_2$H and BaYO$_{3-\delta}$. d) FT-IR spectra of BaScO$_2$H and BaScO$_{3-\delta}$. Calculated spectra for Ba*RE*O$_2$H (*RE* = Y or Sc) are shown for comparison.

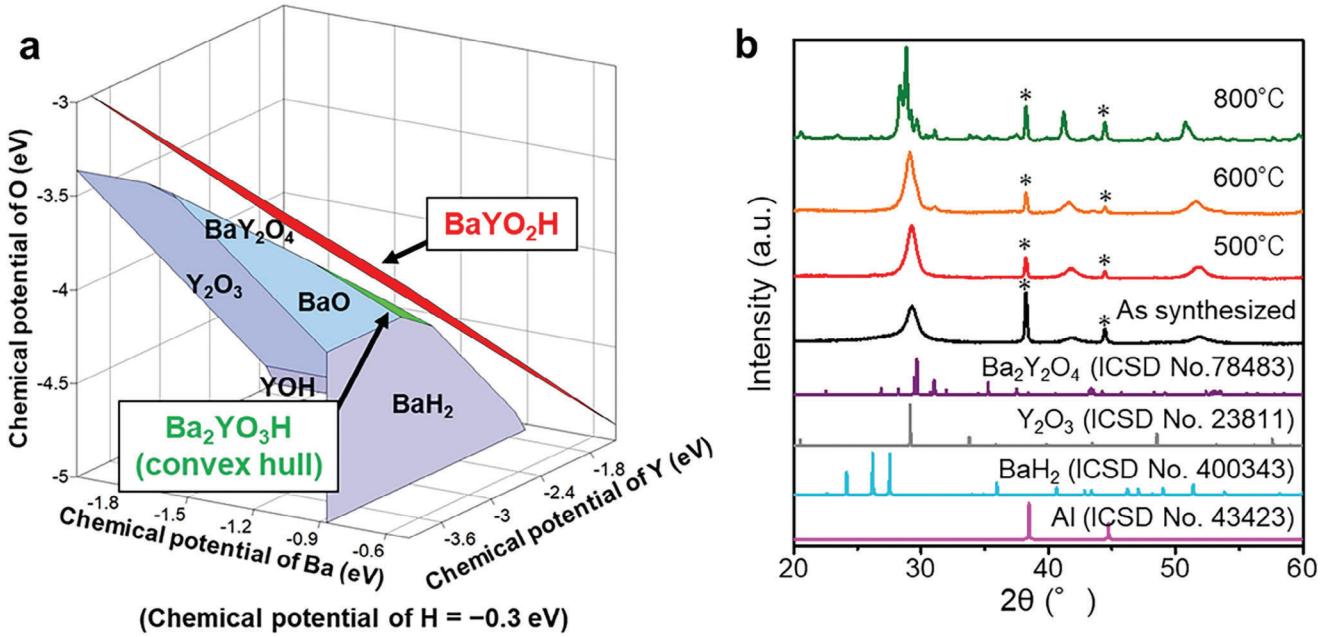

Figure 3. Investigation of the thermodynamic phase stability of $BaYO_2H$. a) Equilibrium phase diagram of the Ba—Y—O—H system at 0 K when the chemical potential of hydrogen is −0.3 eV. b) XRD patterns for $BaYO_2H$ samples after heat treatment at various temperatures under an H_2 atmosphere. The sharp peaks ≈37° and 45° marked by * are attributed to the Al sample holder.

calculated by DFT (Figure S4, Supporting Information). Moreover, it was predicted that the electrons are localized at the hydrogen vacancy sites, which gives rise to a mid-gap state in the bandgap (Figure S5, Supporting Information). These results clearly show the presence of electrons trapped at hydrogen vacancies in the synthesized Ba*RE*O_2H.

Figure 2c,d show FT-IR spectra for Ba*RE*O_2H and Ba*RE*$O_{3-\delta}$ measured in the 400–2000 cm^{-1} region. Based on a comparison with the computational spectra and phonon density of states (Figures S6 and S7, Supporting Information), the broad peaks observed ≈1250 cm^{-1} in the Ba*RE*O_2H spectra are attributed to the hydride vibration mode at the anion sites in the perovskite structure (Figure S8, Supporting Information). In contrast, no such vibration was observed in the Ba*RE*$O_{3-\delta}$ spectra, and only a vibration attributed to the carboxylate structure (O—C═O) ≈1400 cm^{-1} was observed.[26] Therefore, H^- in the Ba*RE*O_2H samples occupies the same anion sites to form metal-hydrogen bonds.

The formation enthalpy (ΔE_F) and the equilibrium phase diagram for the Ba—Y—O—H system at 0 K were predicted from DFT calculations. The ΔE_F for $BaYO_2H$ from BaO, BaH_2, and Y_2O_3 was estimated to be +13.0 kJ mol^{-1}, which indicates that the formation of $BaYO_2H$ is thermodynamically unstable. Moreover, $BaYO_2H$ did not appear on the convex hull in any regions in the Ba—Y—O—H phase diagram, with the chemical potential of hydrogen as the projection axis (Figure S9, Supporting Information). **Figure 3a** shows the Ba—Y—O—H phase diagram, where the hyperplane corresponding to the stable region of $BaYO_2H$ is clearly drawn. The hyperplane is discontinuous with the convex hull, which indicates that $BaYO_2H$ is a metastable phase. When $BaYO_2H$ is heated above 600 °C, it is decomposed to form the raw materials and BaY_2O_4, consistent with its thermodynamic instability (Figure 3b). For this reason, $BaYO_2H$ could not be synthesized by conventional thermal synthesis methods. On the other hand, Ba_2YO_3H can be synthesized by the conventional thermal synthesis method under high-pressure conditions, as predicted from the equilibrium diagram (Figure 3a).[12]

Sirota proposed that a thermodynamically unfavorable reaction can be allowed under a nanostructural excited state caused by strain energy accumulated by mechanical stress and the insertion of atoms into interstitial spaces.[14] Quantitative studies on the accumulation of internal energy using shaker mills and planetary mills have already been performed, which have revealed that internal enthalpies accumulate ≈0.8–10 kJ mol^{-1} for Fe, Al, and AlRu alloys.[27,28] Therefore, the high-energy milling performed in this study enabled the formation of a metastable phase, $BaYO_2H$, with a positive formation enthalpy. On the other hand, the kinetic effects are expected to be important in the formation of $BaScO_2H$ from BaO, BaH_2, and Sc_2O_3 because of its negative formation enthalpy (−26.9 kJ mol^{-1}). The mechanochemical method is expected to be effective toward the inhibition of hydrogen desorption at low temperatures because of the high local pressure caused by mechanical stress, similar to that of a high-pressure synthesis process.[29] Therefore, it would be reasonable for $BaScO_2H$ to form under mechanochemical conditions.

2.2. Catalytic Performance for Ammonia Synthesis

The results have clarified that Ba*RE*O_2H with many hydrogen defects easily releases hydrogen even at low temperatures below 200 °C, which is similar to the reported highly active hydride-based ammonia synthesis catalysts.[30–32] Therefore, the

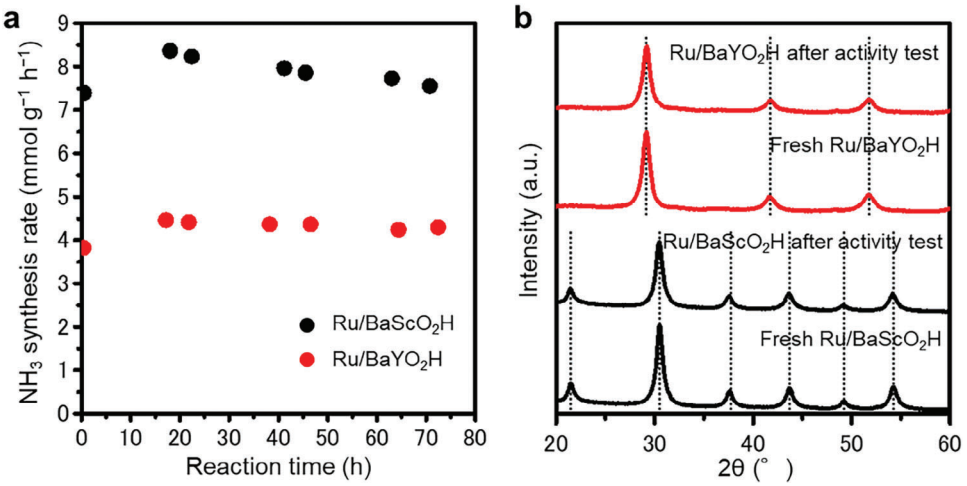

Figure 4. Catalytic stabilities of Ru-loaded Ba*RE*O_2H. a) Stability test for NH_3 synthesis over Ru-loaded Ba*RE*O_2H at 300 °C and 0.9 MPa. b) XRD patterns for Ru/Ba*RE*O_2H before and after ammonia synthesis reaction at 300 °C and 0.9 MPa for 70 h.

synthesized oxyhydrides were applied as catalyst supports of Ru for the ammonia synthesis reaction, and their catalytic properties were evaluated. All catalytic reactions were conducted in a fixed bed flow system as shown in Figure S10 (Supporting Information). The ammonia produced was trapped in an H_2SO_4 solution, and the amount of generated ammonia was quantified using ion chromatography with the calibration curve method (Figures S11,S12, and S13, Supporting Information). The Ru-loaded oxyhydrides worked as catalysts for ammonia synthesis for over 70 h without significant loss of activity (**Figure** 4a). The crystal structures of Ba*RE*O_2H remained unchanged after the reaction (Figure 4b), and of particular note, $BaYO_2H$ exhibited high durability, despite being a metastable phase. XPS measurements were conducted to investigate the chemical stability of these catalysts during ammonia synthesis reactions. Figure S14 (Supporting Information) shows the wide-range XPS spectra of Ru/Ba*RE*O_2H before and after the catalytic reaction. All peaks are assignable to the constituent elements of the catalysts. After the catalytic reaction at 300 °C under 0.9 MPa for 24 h, the Ru $3d_{5/2}$ peaks for Ru/Ba*RE*O_2H shifted to a lower binding energy side than the zero-valent Ru peak (280 eV) observed on original Ru/Ba*RE*O_2H (**Figure** 5a,b). This result suggests that the strong Ru-Ba*RE*O_2H interaction occurs during ammonia synthesis, resulting in electron transfer from Ba*RE*O_2H to Ru. As shown in Figure 5c,d, both Sc $2p_{3/2}$ and Y $3d_{5/2}$ peaks shift to lower binding energy after the catalytic reaction, which may be due to the reduction of metal cation sites by replacing lattice O^{2-} with H^- ions or by forming hydrogen vacancy sites. Anyway, the catalyst surface was not oxidized during the reaction, and therefore, the Ru/Ba*RE*O_2H exhibited stable catalytic activity (Figure 4a).

Figure 6a shows the temperature dependence of the ammonia synthesis rate over various Ru catalysts at 0.9 MPa. The Ru-loaded oxyhydrides exhibited higher activity than the Ru-loaded oxides over the entire temperature range of 200–400 °C. Ru/$BaScO_2H$ showed the highest catalytic performance among the Ru catalysts measured in this study (**Table** 2). Figure 6b summarizes the ammonia synthesis rates and apparent activation energies for the various catalysts (Figures S15 and S16, Supporting Information). The activities of the Ru/Ba*RE*O_2H catalysts were superior to the conventional oxide-supported Ru catalysts with comparable or higher catalytic activities than those of other oxyhydride-based Ru catalysts such as Ru/$BaAl_2O_{4-x}H_y$.[33] The apparent activation energies for Ru/Ba*RE*O_2H (49–67 kJ mol^{-1}) are clearly lower than those for conventional Ru catalysts (120 kJ mol^{-1}) and Ru/Ba*RE*$O_{3-\delta}$ (88–91 kJ mol^{-1}), and close to those for the electride- and hydride-based catalysts (45–69 kJ mol^{-1}).[31–33] These electride and hydride supports have strong promoting effects that lower the energy barrier for ammonia synthesis on Ru; therefore, the results indicate that the Ba*RE*O_2H supports also have such promoting effects.

2.3. Analysis of Reaction Kinetics and Surface Electronic Properties

Kinetic analyses were conducted to obtain information on the reaction mechanism for ammonia synthesis. **Table** 3 summarizes the reaction orders with respect to N_2, H_2, and NH_3 (Figure S17, Supporting Information). The N_2 orders were close to +1 or higher for all the catalysts, which suggests that the rate-determining step is still the dissociation of N_2. In contrast, there was a significant difference in the H_2 orders between the oxide and oxyhydride supports; positive H_2 orders were obtained with Ru/Ba*RE*O_2H, whereas negative H_2 orders were obtained with Ru/Ba*RE*$O_{3-\delta}$, as for conventional Ru catalysts. Conventional Ru catalysts exhibit negative H_2 orders because adsorption of dissociated H_2 prevents N_2 adsorption on the active sites on Ru at high H_2 pressure.[34] Therefore, the positive H_2 orders for Ru/Ba*RE*O_2H indicate that these catalysts overcome such hydrogen poisoning. The NH_3 orders for Ru/Ba*RE*O_2H are largely more negative than Ru/Ba*RE*$O_{3-\delta}$, which indicates that NH_x species derived from the reverse reaction are more densely present on Ru/Ba*RE*O_2H than on Ru/Ba*RE*$O_{3-\delta}$. The accumulated NH_x species may prevent H_2 adsorption, which has an

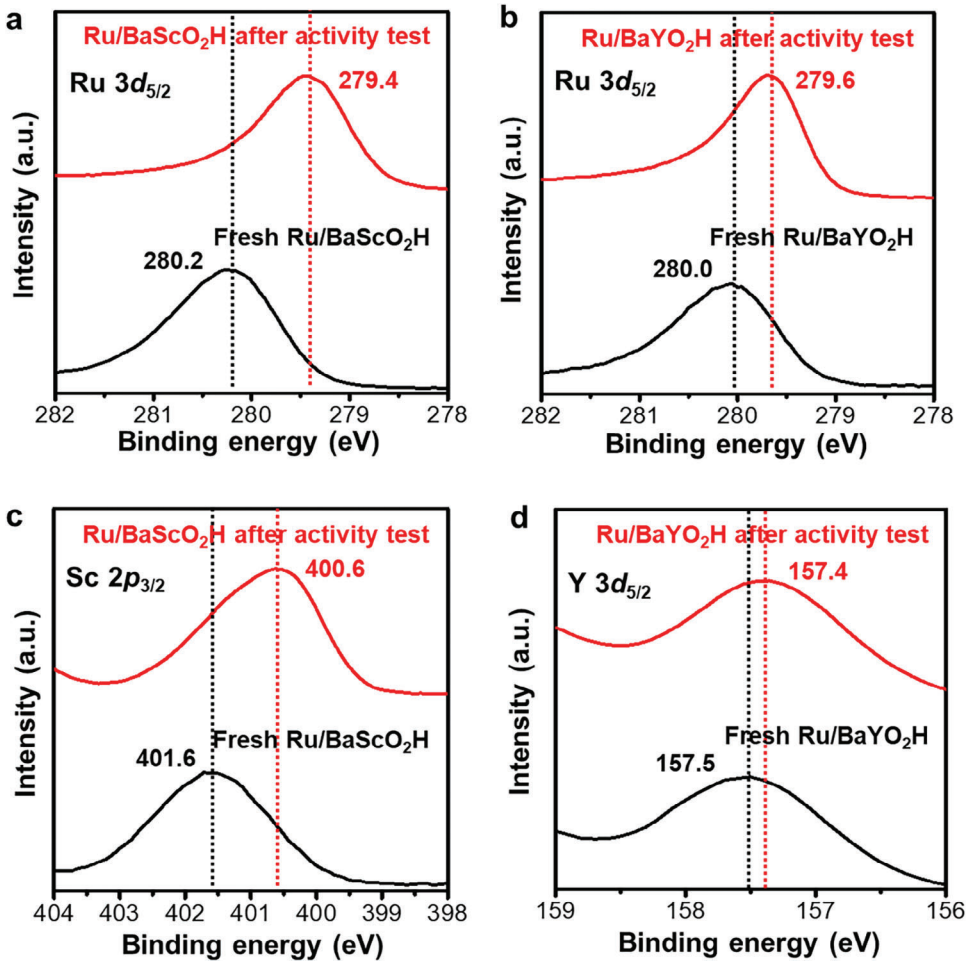

Figure 5. Chemical states of Ru/BaREO_2H surface before and after ammonia synthesis reaction. XPS spectra for Ru $3d_{5/2}$ of a) Ru/$BaScO_2H$ and b) Ru/$BaYO_2H$. c) XPS spectra for Sc $2p_{3/2}$ of Ru/$BaScO_2H$. d) XPS spectra for Y $3d_{5/2}$ of Ru/$BaYO_2H$.

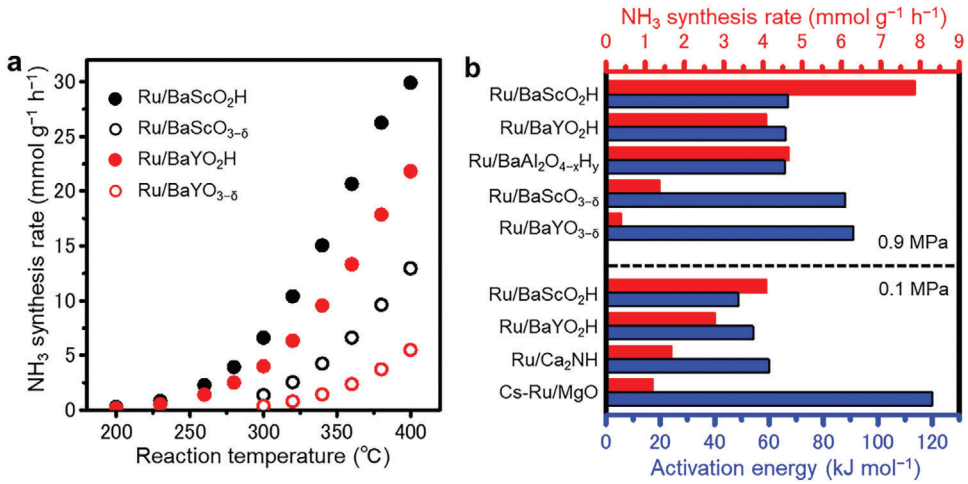

Figure 6. Comparison of catalytic activities. a) Temperature dependence of NH_3 synthesis activity for BaREO_2H and Ba$REO_{3-\delta}$ with Ru metal at 0.9 MPa. b) NH_3 synthesis rates and apparent activation energies for various Ru catalysts at 300 °C and 0.1 MPa (lower part), and at 0.9 MPa (top part).

Table 2. Catalytic performance of various Ru catalysts measured in this work.

Catalyst	S_{BET} [a] [$m^2\ g^{-1}$]	Ru loading [b] [wt.%]	Pressure [MPa]	r_{NH3} [c] [mmol $g^{-1}\ h^{-1}$]	E_a [d] [kJ mol^{-1}]
$Ru/BaYO_2H$	2.2	1.8	0.1	2.77	66.0
			0.9	4.35	54.2
$Ru/BaScO_2H$	4.4	1.7	0.1	4.09	66.8
			0.9	7.87	48.9
$Ru/BaYO_{3-\delta}$	–	1.5	0.9	0.39	91.0
$Ru/BaScO_{3-\delta}$	–	1.7	0.9	1.36	88.0

[a] Specific surface area of various support materials determined by BET analysis; [b] Determined by XRF; [c] Ammonia synthesis rate measured at 300 °C; [d] Activation energy for ammonia synthesis was estimated from Arrhenius plots in the temperature range of 200—400 °C.

Table 3. Reaction order for various Ru catalysts measured at 0.9 MPa.

Catalyst	Temperature [°C]	N_2 order (α)	H_2 order (β)	NH_3 order (γ)	Refs.
$Ru/BaYO_2H$	300	+1.20	+0.34	−1.20	This work
$Ru/BaScO_2H$	300	+1.05	+0.30	−0.83	This work
$Ru/BaYO_{3-\delta}$	320	+1.08	−0.04	−0.32	This work
$Ru/BaScO_{3-\delta}$	320	+1.47	−0.09	−0.42	This work
$Ru/BaAl_2O_{4-x}H_y$	340	+0.72	+1.02	−1.00	[33]

influence on the positive H_2 order.[35] However, the H_2 orders for the oxyhydride-supported Ru catalysts cannot be simply explained by the NH_3 orders. For example, $Ru/BaYO_2H$ with a larger negative NH_3 order shows a smaller H_2 order than $Ru/BaAl_2O_{4-x}H_y$ catalysts. Accordingly, other factors would contribute to the positive H_2 orders for the $Ru/BaREO_2H$ catalysts. Positive H_2 orders have been reported for electride- and hydride-supported Ru catalysts,[30–32] where reversible exchange between anionic electrons and H^- occurs at the metal-support interface, which leads to a high tolerance toward H_2 poisoning. $BaREO_2H$ has a large amount of H^- vacancies so that H adatoms on the Ru surface can react with electrons at the anion vacancies to form H^-. Subsequently, the regeneration of anion vacancies occurs when H^- reacts with nitrogen adsorbed on the Ru surface or desorbs as H_2 from the support surface, and this cycle is expected to suppress hydrogen poisoning. Therefore, we tentatively consider that the above mechanism suppresses hydrogen poisoning on $Ru/BaREO_2H$, which results in high ammonia synthesis rates, even at temperatures as low as 300 °C.

Furthermore, the superior catalytic activity of $Ru/BaREO_2H$ can be explained by the electron-donating properties of the oxyhydride supports. Nitrogen bond dissociation has been reported to be promoted in electride- and hydride-supported Ru catalysts by the enhancement of electron donation to the antibonding orbital of N_2 adsorbed on Ru, which is attributed to the charge transfer of loosely bound electrons at the support surface to Ru.[30,32] **Figure 7a** shows the work functions (WFs) for the most stable surfaces of $BaREO_2H$ and $BaREO_{3-\delta}$ (Table S3 and Figures S18,S19, S20, and S21, Supporting Information). The WFs for $BaScO_2H$ and $BaYO_2H$ for the most stable surface without anion vacancies predicted by DFT calculations are respectively 3.2 eV and 4.2 eV, which are similar to those for $BaScO_{3-\delta}$ and $BaYO_{3-\delta}$. However,

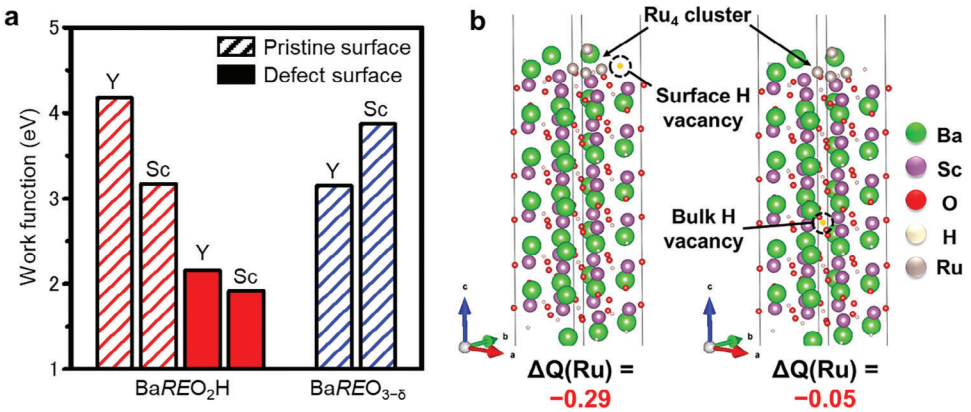

Figure 7. Surface electronic properties. a) WFs of $BaREO_2H$ and $BaREO_{3-\delta}$. b) The most stable geometrical configurations of Ru_4 cluster on $BaScO_2H(100)$ surface with hydrogen vacancy with electrons on the surface (left) and the bulk (right). ΔQ(Ru) represents the Bader charge on the Ru_4 cluster.

the WFs for $BaScO_2H$ and $BaYO_2H$ were significantly decreased by the formation of H vacancies on the top surface, and the lowest WFs were 1.9 and 2.2 eV, respectively. These values are comparable to that for C12A7:e^- (2.4 eV), which has been experimentally confirmed to exhibit high electron donation ability to Ru and N_2 on Ru.[30,36] As additional information, the surface hydrogen vacancy formation energy ΔE_{VH}, at the most stable surfaces was 0.69–1.31 eV for $BaScO_2H$ and 0.51–1.25 eV for $BaYO_2H$ (Table S3, Supporting Information), which are close to the reported values for Ca_2NH and CaH_2 (0.88–1.11 eV) that are predicted to exhibit low WFs (2.3 eV) by the formation of H vacancies.[32,37] These calculation results indicate that Ba*RE*O_2H exhibits high electron-donating properties due to easily formed H vacancies. TDS results also support the ease of hydrogen vacancy formation. The electron-donating ability of Ba*RE*O_2H to Ru was experimentally confirmed by the XPS measurements. As shown in Figure 5a,b, the Ru $3d_{5/2}$ peak of Ru/Ba*RE*O_2H after the catalytic reaction appears at a lower binding energy side than that of metallic Ru (280.0 eV).[38] This is clear experimental evidence for the electron transfer from the oxyhydride support to Ru. In particular, the Ru $3d_{5/2}$ peak for Ru/$BaScO_2H$ (279.4 eV) was located at a lower binding energy side than that for Ru/$BaYO_2H$ (279.6 eV), meaning that $BaScO_2H$ has higher electron donating ability than $BaYO_2H$. As shown in Table S4 (Supporting Information), there is no significant difference in the particle size of Ru between Ru/$BaScO_2H$ and Ru/$BaYO_2H$, which indicates that the superior catalytic activity of Ru/$BaScO_2H$ is not due to the dispersibility of Ru. Therefore, the efficient electron donation ability of $BaScO_2H$ accounts for the superior catalytic activity of Ru/$BaScO_2H$ than that of Ru/$BaYO_2H$. Additional DFT calculations were performed on the Ru-loaded model to investigate the electron-donating properties of $BaScO_2H$ to Ru in detail (Figure S22, Supporting Information). Figure 7b shows the charge transfer between Ru cluster and $BaScO_2H$, which indicates that the electron donation from the surface hydrogen vacancy with electrons is more efficient than that from the bulk hydrogen vacancy. The ΔE_{VH} in the bulk models of $BaScO_2H$ (1.50 eV) is much larger than the surface ΔE_{VH}, which means that the hydrogen vacancies are formed more easily on the surface than in the bulk. Therefore, the high electron-donating ability of $BaScO_2H$ mainly originates from the surface hydrogen vacancies. Moreover, the amount of hydrogen vacancies in $BaScO_2H$ is more than three times higher than that of $BaAl_2O_{4-x}H_y$ (Table S4, Supporting Information). Given the similar Ru particle size between these two catalysts, their activity difference is attributed to the difference in the electron-donating ability between $BaScO_2H$ and $BaAl_2O_{4-x}H_y$. We consider that these electron donation properties of Ba*RE*O_2H contribute to the promotion of N_2 cleavage over Ru, which reduces the activation barrier for ammonia synthesis (49–67 kJ mol^{-1}). From these results, the reaction mechanism of ammonia synthesis over Ru/Ba*RE*O_2H is illustrated in **Figure 8**. The Ba*RE*O_2H support has numerous hydrogen vacancy sites (Figure 2), among which the surface hydrogen vacancies mainly contribute to electron donation into Ru nanoparticles to form negatively charged Ru sites (Figure 5a,b, and Figure 7b). N_2 dissociation is facilitated on negatively charged Ru nanoparticles on Ba*RE*O_2H. The surface hydrogen vacancy sites can capture the hydrogen atoms on the Ru surface, preventing hydrogen poisoning on the Ru surface (Table 3). The surface lattice

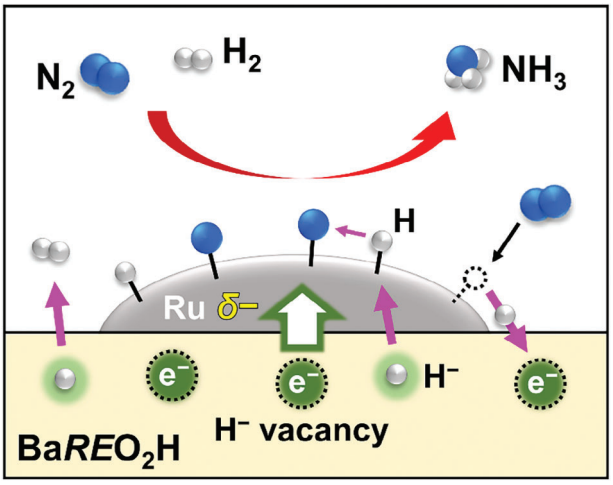

Figure 8. Schematic illustration of ammonia synthesis over Ru/Ba*RE*O_2H.

H^- ions react with nitrogen species on the Ru surface, and at the same time, hydrogen vacancy sites are regenerated at the Ru-support interface. Thus, the reversible exchange between anionic electrons and H^- takes place at the Ru-Ba*RE*O_2H support interface. As a result, nonstoichiometric Ba*RE*$O_{2-x}H_x$ is preserved during ammonia synthesis as confirmed by TDS experiments (Figure S23, Supporting Information).

3. Conclusion

Mechanochemical synthesis of perovskite-type oxyhydrides $BaYO_2H$ and $BaScO_2H$ was successfully achieved. In particular, $BaYO_2H$, which is a metastable phase with a thermodynamically unstable crystal framework, could be synthesized only by the mechanochemical method. The synthesized oxyhydrides were used as supports for ammonia synthesis catalysts that exhibited high catalytic performance comparable to those of previously reported efficient support materials at low temperatures. The high catalytic performance is attributed to the inhibition of hydrogen poisoning at the active sites and the high electron-donating ability induced by H^- vacancies formed on the oxyhydrides. These results are expected to encourage further syntheses of metastable oxyhydrides and the development of promising catalyst supports for ammonia synthesis.

4. Experimental Section

Synthesis of Support Materials: BaO (99.99%, Sigma–Aldrich), BaH_2, Y_2O_3 (99.99%, Kojundo), and Sc_2O_3 (>99.9%, Kojundo) were used as starting materials for the synthesis of the Ba*RE*O_2H (*RE* = Y, Sc) oxyhydrides. BaH_2 was prepared by heating Ba metal (99.99%, Sigma–Aldrich) under an H_2 (>99.99%) atmosphere at 600 °C for 12 h. The mechanochemical synthesis was conducted with reference to a previously reported method for the synthesis of oxyhydrides.[18,19] The starting materials (total weight:2 g, BaO:BaH_2:RE_2O_3 = 1:1:1 molar ratio) were added to a 20 mL grinding bowl made of WC with ten balls (10 mm diameter) under an Ar atmosphere. Mechanochemical synthesis was then conducted using a planetary ball mill (Pulverisette 7 Premium Line, Fritsch) at a speed of 800 rpm for a total of 120 cycles (4 times 30 cycles). One cycle consisted of 2 min of milling and 3 min pauses to reduce the heating of the sample. After 30 cycles, the sample was removed from the grinding bowl and

crushed using an agate mortar. A yttrium-stabilized zirconia grinding bowl and balls were also available and when used, the number of reaction cycles was increased, typically to ≈240–300 cycles at a speed of 850 rpm. To examine the crystal structure, the crystallinity of the milled sample was improved by annealing in an evacuated glass tube at 500 °C for 72 h. The synthesized compounds were highly air-sensitive; therefore, they were stored and handled in an Ar-filled glove box.

Ba*RE*$O_{3-\delta}$ oxides were also synthesized using the same procedure for the synthesis of Ba*RE*O_2H (total weight:2 g, BaO:RE_2O_3 = 2:1 molar ratio). Mechanochemical synthesis was conducted at a speed of 850 rpm for a total of 90–150 cycles (3–5 times 30 cycles). An annealing process was also conducted using the same conditions as those for Ba*RE*O_2H.

Preparation of Catalysts and Catalytic Reaction: $Ru_3(CO)_{12}$ (99%, Sigma–Aldrich) was used as the Ru precursor for Ru/Ba*RE*O_2H and Ru/Ba*RE*$O_{3-\delta}$. The amount of Ru was fixed at 2 wt.%, and Ru loading was conducted according to a previously reported method.[32] The actual amount of Ru loaded on the support was determined by X-ray fluorescence spectroscopy (S8 TIGER, Bruker).

Ammonia synthesis was conducted in a stainless-steel reactor with the catalyst (0.1 g) under a flow of N_2 (purity >99.99995%, 15 mL min^{-1}) and H_2 (purity >99.99999%, 45 mL min^{-1}) with a H_2/N_2 flow ratio of 3 at 200–400 °C and 0.1–0.9 MPa. The ammonia produced was trapped in an H_2SO_4 solution, and the amount of NH_4^+ ions generated in the solution was determined using ion chromatography (Prominence, Shimadzu) with a conductivity detector. The apparent activation energies were calculated from Arrhenius plots of the ammonia synthesis rates at various temperatures. Ammonia synthesis rates that were less than ca. 15% of the equilibrium conversion were used to evaluate the apparent activation energies.

Kinetic Analysis: The reaction orders of the catalysts were measured using a previously reported method.[39] The reaction orders with respect to N_2 (α) and H_2 (β) were calculated from the gas partial pressure dependence on the ammonia synthesis rate at a constant flow rate of mixed gas of Ar, H_2, and N_2 (60 mL min^{-1}). The catalyst (0.1 g) was kept at 0.9 MPa and at a temperature where the outlet ammonia concentration was less than 10% of the equilibrium conversion. The ammonia synthesis rate (r) over various catalysts can be expressed by a power law equation using the partial pressures of nitrogen (P_{N2}), hydrogen (P_{H2}), and ammonia (P_{NH3}):

$$r = k P_{N2}^{\alpha} P_{H2}^{\beta} P_{NH3}^{\gamma} \quad (1)$$

where k is a rate constant, and α, β, γ are the reaction orders with respect to N_2, H_2, and NH_3, respectively. The reaction orders were calculated using Equations. (1–5):

$$r = \left(\frac{1}{W}\right) \mathrm{d}y_0/\mathrm{d}\,(1/q) \quad (2)$$

$$\log\, y_0 = log\left(\frac{C}{q}\right)^{1/m} \quad (3)$$

$$r = \left(\frac{1}{W}\right)\left(\frac{C}{m}\right) y_0^{1-m} \quad (4)$$

$$C = k_2 P_{N2}^{\alpha} P_{H2}^{\beta} \quad (5)$$

where y_0, W, q, (1–m) and k_2 represent the mole fraction of outlet ammonia, the weight of the catalyst, the total flow rate, the NH_3 order (γ), and the rate constant respectively.

Characterization: The crystal structures of the oxyhydrides were identified using powder X-ray diffraction (XRD; MiniFlex600, Rigaku) with Cu Kα radiation (λ = 0.15418 nm). The sample was sealed in an X-ray transmitting container to protect it from oxidation and hydration. Rietveld refinements were performed using the TOPAS (Bruker AXS, version 4.2) software. Hydrogen desorption from the support materials was detected using thermal desorption spectroscopy (TDS; TDS-1400TV, ESCO). Powder samples placed on a SiO_2 holder were heated to 1200 °C under vacuum conditions, and desorbed hydrogen ions (m/z = 2) and water ions (m/z = 18) were counted as an electronic current by a quadrupole mass spectrometer. The numbers of hydrogen molecules and water molecules were calculated based on the area of the desorption peak corrected using a silicon wafer containing implanted hydrogen. The Brunauer–Emmett–Teller (BET) specific surface area of the oxyhydrides was obtained from nitrogen adsorption isotherms measured at liquid-nitrogen temperature using an automatic gas adsorption instrument (BELSORP-mini II, MicrotracBEL). The vibrational spectra were recorded with a Fourier transform infrared spectrometer (FT-IR; Frontier DTGS, PerkinElmer). The samples were sealed in KBr plates to avoid oxygen and water contamination. Measurements were conducted between 4000 and 500 cm^{-1} with a spectral resolution of 4 cm^{-1}. Optical diffuse reflectance spectra were measured at room temperature with an UV–vis spectrometer (UV–vis; U-4000, Hitachi). X-ray photoelectron spectroscopy (XPS; KRATOS ULTRA2, Shimadzu) was conducted using an apparatus equipped with a charge neutralization system. The binding energy of all spectra was calibrated with reference to the C 1s peak. All samples were delivered from the Ar-filled glovebox to the XPS analysis chamber through the vacuum transfer chamber to avoid oxidation and decomposition of the sample surface upon contact with air. The average particle size of Ru was determined by CO pulse chemisorption at 50 °C with a He flow of 30 mL min^{-1} and 0.031 mL pulses of 9.51% CO in He using a catalyst analyzer (BELCAT-A, MicrotracBEL); spherical metal particles and a stoichiometry of Ru/CO = 1 were assumed.

DFT Calculations: Density functional theory (DFT) calculations were conducted using the Vienna Ab initio Simulation Package (VASP) code.[40,41] The electron exchange and correlation were described using a Perdew–Burke–Ernzerhof type generalized gradient approximation.[42] The $5s^2$, $5p^6$, and $6s^2$ electrons of Ba, $4s^2$, $4p^6$, and $5s^2$ electrons of Y, $3s^2$, $3p^6$, and $4s^2$ electrons of Sc, $2s^2$ and $2p^4$ electrons of O, $1s^1$ electron of H, and $4p^6$, $5s^2$, and $4d^6$ electrons of Ru were handled as valence electrons. The core electrons were described using the projector augmented wave (PAW) method.[43,44] A cutoff energy of 550 eV for BaYO_2H and 500 eV for BaScO_2H were used. 4 × 4 × 7 k-point meshes were used for structural optimization of the bulk, while the Γ-point-only approach was applied for the slab. Electrostatic potentials applied for evaluation of the WF were calculated using 2 × 3 × 1 k-point meshes for the optimized slab models. The convergence criteria for energy and force were respectively 1.0 × 10^{-5} eV and 1.0 × 10^{-2} eV Å^{-1} for other than phonon calculations. For the phonon calculations, 7 × 7 × 15 k-point meshes were used and convergence criteria of 1.0 × 10^{-6} eV and 1.0 × 10^{-4} eV Å^{-1} were used for energy and force, respectively. To determine the stable anion arrangement of Ba*RE*O_2H with the lowest energy, 35 structures with different anion arrangements in a 2 × 2 × 1 supercell based on a cubic unit cell were generated using the Supercell program and optimized.[45] Stable structures of oxygen-deficient perovskite Ba*RE*$O_{3-\delta}$ were also determined by the same procedure as that for Ba*RE*O_2H. The composition of Ba*RE*$O_{3-\delta}$ was assumed to be Ba*RE*$O_{2.5}$ to satisfy the charge neutrality. Phonon calculations were performed based on the finite displacement method, and the displaced structures were generated using the Phonopy module.[46] IR spectra with fixed line widths of 16.5 cm^{-1} were calculated using the Phonopy-Spectroscopy package.[47] Slab models with non-polar and stoichiometric surfaces were generated by the tsubo.pl, module with primitive cells of the structure with the most stable anion arrangement as the input.[48,49] The slabs were constructed in 13 atomic layers, and a 20 Å vacuum layer was introduced between the slabs to eliminate the interactions between the slabs. Surface energies were calculated for all optimized slab models and the most stable facets were determined as (111) for BaYO_2H, (100) for BaScO_2H, (010) for Ba$YO_{2.5}$, and (111) for Ba$ScO_{2.5}$. The formation enthalpies for the Ba*RE*O_2H oxyhydrides ΔE_F, at 0 K were defined as $2E(\mathrm{BaRE O_2H}) - \{E(\mathrm{BaO}) + E(\mathrm{BaH_2}) + E(\mathrm{RE_2O_3})\}$, where E is the total energy per compositional formula. Structural information for various phases that contained the elements of Ba, Y, O, and H was obtained from the ICSD and Materials Project databases. The formation enthalpies for each element were calculated after optimization of all the structures, and the equilibrium phase diagram for the Ba—Y—O—H system was created using the Chesta program with the calculated enthalpies. The WF was defined as the difference between the Fermi energy for the slab models and the electrostatic potential in the vacuum gap of the slab model. We used a

Bader analysis of the charge density distributions for an atomic charge.[50] All crystal structures for the bulk and slab models were visualized using the VESTA software package.[51]

Supporting Information

Supporting Information is available from the Wiley Online Library or from the author.

Acknowledgements

This work was supported by the FOREST Program (No. JPMJFR203A), the JST-Mirai Program (JPMJMI21E9) and the JST SPRING (No. JPMJSP2106) of the Japan Science and Technology Agency (JST), the Kakenhi Grant-in-Aid (No. JP22H00272, JP24H02204) from the Japan Society for the Promotion of Science (JSPS), and the Tokyo Tech Advanced Researchers [STAR] Grant funded by the Tokyo Institute of Technology Fund (Tokyo Tech Fund).

Conflict of Interest

The authors declare no conflict of interest.

Data Availability Statement

The data that support the findings of this study are available from the corresponding author upon reasonable request.

Keywords

ammonia synthesis, mechanochemical method, metastable oxyhydride, Ru-based catalyst

Received: May 31, 2024
Revised: July 11, 2024
Published online: August 3, 2024

[1] K. Fukui, S. Iimura, A. Iskandarov, T. Tada, H. Hosono, *J. Am. Chem. Soc.* **2022**, *144*, 1523.
[2] T. Wu, A. Ishikawa, T. Honda, H. Tamatsukuri, K. Ikeda, T. Otomo, S. Matsuishi, *RSC Adv.* **2019**, *9*, 5282.
[3] Y. Tang, Y. Kobayashi, N. Masuda, Y. Uchida, H. Okamoto, T. Kageyama, S. Hosokawa, F. Loyer, K. Mitsuhara, K. Yamanaka, Y. Tamenori, C. Tassel, T. Yamamoto, T. Tanaka, H. Kageyama, *Adv. Energy Mater.* **2018**, *8*, 1801772.
[4] M. Miyazaki, K. Ogasawara, T. Nakao, M. Sasase, M. Kitano, H. Hosono, *J. Am. Chem. Soc.* **2022**, *144*, 6453.
[5] Y. Kobayashi, O. J. Hernandez, T. Sakaguchi, T. Yajima, T. Roisnel, Y. Tsujimoto, M. Morita, Y. Noda, Y. Mogami, A. Kitada, M. Ohkura, S. Hosokawa, Z. Li, K. Hayashi, Y. Kusano, J. eun Kim, N. Tsuji, A. Fujiwara, Y. Matsushita, K. Yoshimura, K. Takegoshi, M. Inoue, M. Takano, H. Kageyama, *Nat. Mater.* **2012**, *11*, 507.
[6] K. Fukui, S. Iimura, T. Tada, S. Fujitsu, M. Sasase, H. Tamatsukuri, T. Honda, K. Ikeda, T. Otomo, H. Hosono, *Nat. Commun.* **2019**, *10*, 2578.
[7] K. Hayashi, P. V. Sushko, Y. Hashimoto, A. L. Shluger, H. Hosono, *Nat. Commun.* **2014**, *5*, 3515.
[8] G. Kobayashi, Y. Hinuma, S. Matsuoka, A. Watanabe, M. Iqbal, M. Hirayama, M. Yonemura, T. Kamiyama, I. Tanaka, R. Kanno, *Science* **2016**, *351*, 1314.
[9] A. Mutschke, A. Schulz, M. Bertmer, C. Ritter, A. J. Karttunen, G. Kieslich, N. Kunkel, *Chem. Sci.* **2022**, *13*, 7773.
[10] Y. Kobayashi, O. Hernandez, C. Tassel, H. Kageyama, *Sci. Technol. Adv. Mater.* **2017**, *18*, 905.
[11] J. Schmidt, L. Pettersson, C. Verdozzi, S. Botti, M. A. L. Marques, *Sci. Adv.* **2021**, *7*, eabi7948.
[12] H. Nawaz, F. Takeiri, A. Kuwabara, M. Yonemura, G. Kobayashi, *Chem. Commun.* **2020**, *56*, 10373.
[13] W. Kwestroo, H. A. M. van Hal, C. Langereis, *Mater. Res. Bull.* **1974**, *9*, 1631.
[14] N. N. Sirota, *Met. Sci. Heat Treat.* **2005**, *47*, 531.
[15] J. Huot, D. B. Ravnsbæk, J. Zhang, F. Cuevas, M. Latroche, T. R. Jensen, *Prog. Mater. Sci.* **2013**, *58*, 30.
[16] M. Paskevicius, L. H. Jepsen, P. Schouwink, R. Černý, D. B. Ravnsbæk, Y. Filinchuk, M. Dornheim, F. Besenbacher, T. R. Jensen, *Chem. Soc. Rev.* **2017**, *46*, 1565.
[17] T. Uchimura, F. Takeiri, K. Okamoto, T. Saito, T. Kamiyama, G. Kobayashi, *J. Mater. Chem. A* **2021**, *9*, 20371.
[18] A. Mutschke, T. Wylezich, C. Ritter, A. J. Karttunen, N. Kunkel, *Eur. J. Inorg. Chem.* **2019**, *2019*, 5073.
[19] T. Wylezich, R. Valois, M. Suta, A. Mutschke, C. Ritter, A. Meijerink, A. J. Karttunen, N. Kunkel, *Chem. – Eur. J.* **2020**, *26*, 11742.
[20] L. Yang, Z. Pan, Z. Tian, *ChemCatChem* **2024**, *16*, 202301519.
[21] Y. Sasahara, R. Terada, H. Ubukata, M. Asahi, D. Kato, T. Tsumori, M. Namba, Z. Wei, C. Tassel, H. Kageyama, *J. Am. Chem. Soc.* **2024**, *146*, 11694.
[22] Y. Goto, C. Tassel, Y. Noda, O. Hernandez, C. J. Pickard, M. A. Green, H. Sakaebe, N. Taguchi, Y. Uchimoto, Y. Kobayashi, H. Kageyama, *Inorg. Chem.* **2017**, *56*, 4840.
[23] R. P. Liferovich, R. H. Mitchell, *J. Solid State Chem.* **2004**, *177*, 2188.
[24] M. Bharathy, A. H. Fox, S. J. Mugavero, H.-C. zur Loye, *Solid State Sci.* **2009**, *11*, 651.
[25] T. Omata, T. Fuke, S. Otsuka-Yao-Matsuo, *Solid State Ion.* **2006**, *177*, 2447.
[26] P. Du, D. Huo, H. Xi, Y. Kang, X. Sun, D. Xiao, *Ceram. Int.* **2017**, *43*, 9854.
[27] Y. H. Zhao, H. W. Sheng, K. Lu, *Acta Mater.* **2001**, *49*, 365.
[28] E. Hellstern, H. J. Fecht, Z. Fu, W. L. Johnson, *J. Appl. Phys.* **1989**, *65*, 305.
[29] Z. Xie, M. Graule, N. Orlovskaya, E. A. Payzant, D. A. Cullen, R. G. Blair, *J. Solid State Chem.* **2014**, *215*, 16.
[30] M. Kitano, Y. Inoue, Y. Yamazaki, F. Hayashi, S. Kanbara, S. Matsuishi, T. Yokoyama, S.-W. Kim, M. Hara, H. Hosono, *Nat. Chem.* **2012**, *4*, 934.
[31] M. Kitano, S. Kanbara, Y. Inoue, N. Kuganathan, P. V. Sushko, T. Yokoyama, M. Hara, H. Hosono, *Nat. Commun.* **2015**, *6*, 6731.
[32] M. Kitano, Y. Inoue, H. Ishikawa, K. Yamagata, T. Nakao, T. Tada, S. Matsuishi, T. Yokoyama, M. Hara, H. Hosono, *Chem. Sci.* **2016**, *7*, 4036.
[33] Y. Jiang, R. Takashima, T. Nakao, M. Miyazaki, Y. Lu, M. Sasase, Y. Niwa, H. Abe, M. Kitano, H. Hosono, *J. Am. Chem. Soc.* **2023**, *145*, 10669.
[34] S. E. Siporin, R. J. Davis, *J. Catal.* **2004**, *225*, 359.
[35] K. Aika, M. Kumasaka, T. Oma, O. Kato, H. Matsuda, N. Watanabe, K. Yamazaki, A. Ozaki, T. Onishi, *Appl. Catal.* **1986**, *28*, 57.
[36] Y. Toda, H. Yanagi, E. Ikenaga, J. J. Kim, M. Kobata, S. Ueda, T. Kamiya, M. Hirano, K. Kobayashi, H. Hosono, *Adv. Mater.* **2007**, *19*, 3564.
[37] H. Hosono, M. Kitano, *Chem. Rev.* **2021**, *121*, 3121.

[38] K. S. Kim, N. Winograd, *J. Catal.* **1974**, *35*, 66.
[39] M. Kitano, J. Kujirai, K. Ogasawara, S. Matsuishi, T. Tada, H. Abe, Y. Niwa, H. Hosono, *J. Am. Chem. Soc.* **2019**, *141*, 20344.
[40] G. Kresse, J. Furthmüller, *Phys. Rev. B* **1996**, *54*, 11169.
[41] G. Kresse, J. Furthmüller, *Comput. Mater. Sci.* **1996**, *6*, 15.
[42] J. P. Perdew, K. Burke, M. Ernzerhof, *Phys. Rev. Lett.* **1996**, *77*, 3865.
[43] P. E. Blöchl, *Phys. Rev. B* **1994**, *50*, 17953.
[44] G. Kresse, D. Joubert, *Phys. Rev. B* **1999**, *59*, 1758.
[45] K. Okhotnikov, T. Charpentier, S. Cadars, *J. Cheminformatics* **2016**, *8*, 17.
[46] A. Togo, I. Tanaka, *Scr. Mater.* **2015**, *108*, 1.
[47] J. M. Skelton, L. A. Burton, A. J. Jackson, F. Oba, S. C. Parker, A. Walsh, *Phys. Chem. Chem. Phys.* **2017**, *19*, 12452.
[48] Y. Hinuma, Y. Kumagai, F. Oba, I. Tanaka, *Comput. Mater. Sci.* **2016**, *113*, 221.
[49] Y. Hinuma, Y. Kumagai, I. Tanaka, F. Oba, *Phys. Rev. Mater.* **2018**, *2*, 124603.
[50] W. Tang, E. Sanville, G. Henkelman, *J. Phys. Condens. Matter* **2009**, *21*, 084204.
[51] K. Momma, F. Izumi, *J. Appl. Crystallogr.* **2011**, *44*, 1272.